Metamagnetic tricritical behavior of the magnetic topological insulator $MnBi_4Te_7$

Hui Zhang [1,2] Hengheng Wu [1,2] Daheng Liu,[1,2] Jianqi Huang,[1] Fei Gao,[1,2] Teng Yang [1,2] Xinguo Zhao,[1,2,*] Bing Li,[1,2] Song Ma [1,2,†] and Zhidong Zhang [1,2]

[1] *Shenyang National Laboratory for Materials Science, Institute of Metal Research, Chinese Academy of Sciences, 72 Wenhua Road, Shenyang 110016, China*

[2] *School of Materials Science and Engineering, University of Science and Technology of China, Shenyang 110016, China*

(Received 16 January 2024; revised 26 May 2024; accepted 31 May 2024; published 20 June 2024)

We report temperature and magnetic field dependences of the magnetization and ac susceptibility of $MnBi_4Te_7$, aiming to construct a magnetic phase diagram for $H \parallel [001]$. Its spin Hamiltonian can be described as an Ising model for a metamagnet. The superlattice structure of $MnBi_2Te_4 \cdot (Bi_2Te_3)_n$ facilitates the reduction of interlayer antiferromagnetic interaction. As predicted by the model, there is a tricritical point in the phase diagram when the ratio of the intralayer to interlayer interaction is less than $-3/5$. The tricritical point is determined to be (12.4 K, 660 Oe) by the imaginary part of ac susceptibility due to the dissipation of domain walls of the mixed phase. The effective tricritical exponents, $\beta_2^{\text{eff}} \sim 1.10$, $\delta_2^{\text{eff}} \sim 1.65$, have been obtained and differ from the mean-field exponents. When the logarithmic correction factor $|\ln |t||^{0.5}$ is included, the data collapse with the mean-field power law. These findings were tested against the tricritical scaling hypothesis. The deviation from the Landau theoretical values results from the logarithmic correction, similar to another layered metamagnet $FeCl_2$. As a member of the intrinsic magnetic topological insulator family, $MnBi_4Te_7$ features a tricritical point in its magnetic phase diagram, providing a solid foundation for future research on topological transitions and tricriticality.

DOI: 10.1103/PhysRevB.109.214428

I. INTRODUCTION

The topologically nontrivial band structure and magnetism of $MnBi_2Te_4 \cdot (Bi_2Te_3)_n$ $(n = 0, 1, 2, \ldots)$ have made fundamental issues associated with the quantum Hall effect a subject of much attention [1–20]. Specifically, $MnBi_2Te_4$ ($n = 0$) with A-type antiferromagnetic (AFM) order has realized a quantum anomalous Hall (QAH) insulator and an axion insulator, respectively, in its odd and even layer systems [16,17]. Although topological transitions extend beyond the classical Landau-Ginzburg phase transition theory, the topological phases are enriched by the notion of spontaneous symmetry breaking [21–23]. In the QAH state under zero magnetic field, the spontaneous magnetization induces the chiral edge states at the sample edge as well as at the domain walls [24–26]. The investigation of phase transitions in topological systems are beneficial for understanding novel topological phases.

For critical phenomena accompanied by spontaneous symmetry breaking, the fundamental concept of universality class supplies an effective methodology to investigate and uncover phase transitions [27–35]. The same universality class can be described by equations of states, which generates a series of critical exponents [36]. Tricriticality, as a sibling of criticality, is a fundamental and attractive topic in condensed-matter physics, which reveals competition and balance among multiple phases and interactions [37–39]. Such transition points were envisaged by Landau in 1937 who called them "critical points of a continuous phase transition" [40] and the term tricritical point (TCP) was first proposed by Griffiths in 1970 [41]. In magnetic systems, an antiferromagnet with strong axial anisotropy in a uniform magnetic field near the Néel temperature does not change the property of the critical point [41,42]. However, below a certain temperature and in a sufficiently high field, the transition from the antiferromagnetic to the saturated paramagnetic (SPM) phase, known as the spin-flip transition, is the first order. The magnetic phase diagram depends on the competing interaction ratio $\lambda = J_\parallel / J_\perp$ [43,44]. Notably, when the ratio is less than $-3/5$, a phase diagram with a tricritical point emerges. The range of validity of Landau theory for the tricritical system is estimated by Ginzburg criterion, which indicates that the upper critical dimension d^+ is 3 [45]. This means that these tricritical exponents are expected to take mean-field values for a three-dimensional lattice but require a logarithmic correction at marginal dimensionality [46–48]. The mean-field exponents agree well with measurements on He^3-He^4 mixtures and the dysprosium aluminum garnet (DAG) metamagnet [49–51]. However, there are deviations from the mean-field tricritical exponents, where a fractional power of the logarithmic correction is applied, as observed in the layered metamagnet $FeCl_2$ [52–55].

Here we focus on $MnBi_4Te_7$ $(n = 1)$ with a hexagonal superlattice crystal structure consisting of alternately stacked $MnBi_2Te_4$ a septuple layer (SL) and Bi_2Te_3 a quintuple layer (QL) [2,20,58]. $MnBi_2Te_4$ was evidenced as the first A-type antiferromagnetic topological insulator with ferromagnetic

*Contact author: xgzhao@imr.ac.cn
†Contact author: songma@imr.ac.cn

TABLE I. Experimental and theoretical tricritical exponents.

Material	Author	β_2^+	β_2^-	β_2	β_1	$\delta_2^{\pm a}$	$\gamma_2^{(\pm)b}$	Φ_2
He^3-He^4	Graf *et al*. [51]	$\sim$1	$\sim$1	$\sim$1				
	Leiderer *et al*. [56]						$\sim$1	
	Giordano *et al*. [57]							1.95 ± 0.08
$FeCl_2$	Birgeneau *et al*. [52]	$\sim$1	$\sim$0.36		$\sim$0.19			$\sim$2
	Dillon *et al*. [54]	1 ± 0.02	1 ± 0.07	1 ± 0.08				
	Griffin *et al*. [53]	1.03 ± 0.05	1.13 ± 0.14	1.11 ± 0.11				
DAG	Giordano *et al*. [50]	$\sim$1	$\sim$1	0.98 ± 0.05		2.14 ± 0.26	1.01 ± 0.07	1.95 ± 0.11
$MnBi_4Te_7$	Present work	$\sim$1	$\sim$1	1.02 ± 0.10		1.92 ± 0.28		
Theory	Kincaid *et al*. [44]	1	1	1	0.5	2	1	2

[a]Where δ_2^+ and δ_2^- are the exponents for the paramagnetic and antiferromagnetic phases, respectively, and we give one of them.
[b]Where γ_2^+, γ_2^-, and γ_2 are the exponents along three different phase boundaries and we give one of them.

intralayer interactions $J_\parallel$ and antiferromagnetic interlayer coupling $J_\perp$ [18]. Recently, $MnBi_4Te_7$ was found to exhibit much weaker interlayer interaction than $MnBi_2Te_4$ due to the QL intercalation, resulting in a spin-flip transition rather than a spin-flop transition in the magnetization curve [19]. It is plausible to use the so-called "Ising model for a metamagnet" to describe the magnetic effective Hamiltonian of $MnBi_4Te_7$, which predicts a tricritical point in the magnetic phase diagram. To explore the nature of tricritical phenomena, we have performed two kinds of measurements: high-resolution isothermal static magnetization and ac susceptibility in varying fields along the crystallographic c axis of $MnBi_4Te_7$.

In this work, we constructed a magnetic phase diagram of $MnBi_4Te_7$ and discovered a mixed-phase region terminating at a tricritical point (12.4 K, 660 Oe). Around the tricritical point, we demonstrate that the mean-field exponents, $\beta_2 = 1, \delta_2 = 2$, do not satisfy the scaling relations for our magnetization data. Instead, the predicted behavior aligns with our data only if these exponents are allowed to take effective values, $\beta_2^{\mathrm{eff}} \sim 1.10$, $\delta_2^{\mathrm{eff}} \sim 1.65$. This suggests that the logarithmic factor can be represented by power laws with effective tricritical exponents for the layered metamagnets $FeCl_2$ and our $MnBi_4Te_7$. We have summarized the tricritical exponents of $MnBi_4Te_7$ and the other systems in Table I. $MnBi_4Te_7$ exhibits tricritical behavior and our data on the uniform (nonordering) magnetization are sufficiently precise to permit a careful test of the predictions of tricritical scaling theory discussed in the Appendix.

II. EXPERIMENTAL DETAILS

A. Sample preparation

Single crystals of $MnBi_4Te_7$ were grown using the self-flux method [10,58]. High-purity Mn (powder 99.95%), Bi (grain 99.999%), and Te (lump 99.999%), with starting elements were mixed and the molar ratio of Mn:Bi:Te is 1:10:16. The mixture was loaded in a high-quality alumina crucible, sealed in a quartz tube under high vacuum, heated to 1050 °C, and held for 6 h. After a quick cooling to 600 °C at a rate of 10 °C/h, the mixtures were slowly cooled down to 585 °C over two days. The excess molten liquid flux was separated from the crystals in a centrifuge with silica wool serving as a filter. Although Bi_2Te_3 is the inevitable side product, we can differentiate $MnBi_4Te_7$ pieces by measuring their (00l) diffraction peaks. The phase and quality examinations of the $MnBi_4Te_7$ were performed on a powder crystal x-ray diffractometer with Cu $K\alpha$ radiation ($\lambda = 1.54175$ Å) at room temperature. $MnBi_4Te_7$ single crystals are stable in the air. For magnetic material, its magnetic properties are shape dependent. The standard demagnetizing correction Eq. (1) is only strictly for uniform ellipsoids. As in the case of $MnBi_4Te_7$, the material cannot be shaped. The alternative approach is then to use a thin sample and cut it into an ellipsoidal platelet of dimensions $2 \times 1 \times 0.21$ mm^3 as shown in the inset of Fig. 1(b).

B. Magnetization measurements

High-resolution magnetization measurements were performed with a Magnetic Property Measurement System (MPMS XL-7, Quantum Design). In order to avoid something like magnetocaloric effects affecting the state of the sample, measurements were taken point by point rather than using the sweeping model continuously. Especially, when applying a field and temperature approach to the phase boundary, one should repeat each reading until a consistent value was obtained and the magnetization was determined by means of a standard reciprocating sample option mode. In practice it is possible to take measurements in steps as small as 10 Oe with sufficient accuracy to yield dependable values. We use the standard formula for a demagnetizing correction,

$$H_i = H_a - 4\pi NM, \tag{1}$$

where M is the magnetization, H_a is the applied field, H_i is the internal field, and N is a demagnetizing factor. For our sample the effective demagnetizing factor can be estimated from Fig. S1(b), $N = 0.89$. This was followed by measurement of the ac susceptibility data. The ac field was only turned on while recording the susceptibility data and the ac susceptibility was recorded in the frequency range from 1 Hz to 500 Hz and at the excitation amplitude of 2 Oe.

III. RESULTS AND DISCUSSION

A. Crystal structure and magnetic properties

In this section, we analyze the crystal structure and magnetic properties of $MnBi_4Te_7$ crystals, which form the basis

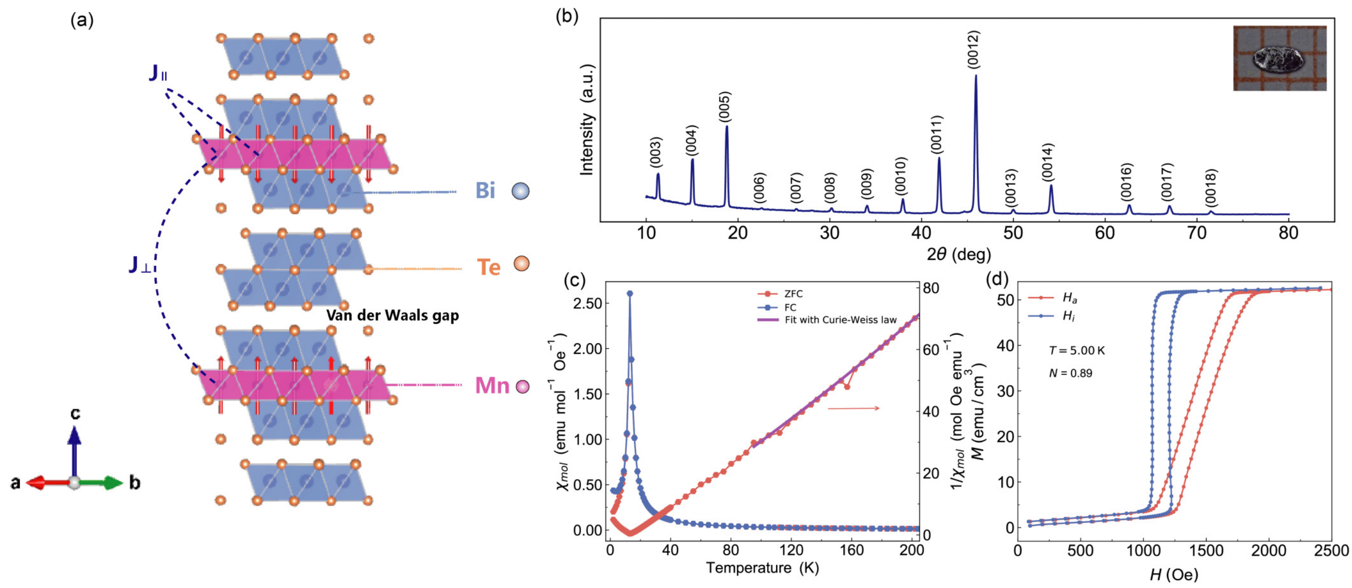

FIG. 1. Crystal structure and magnetic properties of $MnBi_4Te_7$. (a) The view of crystal structure of $MnBi_4Te_7$ from the [110] directions. Blue block: edge-sharing $BiTe_6$ octahedra; pink block: edge-sharing $MnTe_6$ octahedra. Red arrow: magnetic moment directions of Mn ions. $J_\perp$, the interlayer exchange coupling; $J_\parallel$, the intralayer exchange coupling. (b) The $(00l)$ x-ray diffraction peaks of cleaved *ab* plane of $MnBi_4Te_7$. Inset: a piece of $MnBi_4Te_7$ crystal against 1 mm scale. (c) The temperature dependent field-cooled and zero-field-cooled susceptibility and inverse susceptibility taken at $H = 100$ Oe for $H \parallel c$. (d) Magnetic hysteresis loop of isothermal magnetization taken at $T = 5.0$ K and the loop with demagnetizing correction.

for our discussion of the tricritical behavior in Sec. III B. Figure 1(b) shows the $(00l)$ x-ray diffraction peaks of the surface of as-grown single crystals along the crystallographic c axis of $MnBi_4Te_7$, which can be well indexed by the structure proposed in previous reports [10,58]. The $MnBi_4Te_7$ single crystal features a superlatticelike structure material formed by alternating QL and SL layers, as illustrated in Fig. 1(a).

The magnetic properties depicted in Fig. 1(c) present the field-cooled (FC) and zero-field-cooled (ZFC) magnetic susceptibility data measured at $H = 100$ Oe with $H \parallel c$ axis. Abrupt transitions around $T_N = 12.9$ K indicate an intrinsic long range AFM ordering, as shown in Fig. S2(a). As seen from Fig. 1(c) the paramagnetic regime above T_N was fitted with a modified Curie-Weiss law, $\chi(T) = \chi_0 + C/(T - \theta_{CW})$, in the 100 K to 300 K range. The fitted effective paramagnetic moment of $5.0\mu_B$ roughly agrees with the high-spin configuration of Mn^{2+} ($S = 5/2$), and the positive value of the Curie-Weiss temperature ($\theta_{CW} = 11$ K). It is worth mentioning that $MnBi_2Te_4$ has a much higher T_N of 24 K and a lower θ_{CW} of 3 K [1]. This indicates that the AFM exchange interaction of $MnBi_4Te_7$ is significantly weaker than $MnBi_2Te_4$, which is consistent with the fact that the nonmagnetic spacer QL layer reduces the interlayer exchange interaction between adjacent MnTe layers [2,10]. For the two-sublattice antiferromagnet in molecular field theory, the ratio of intralayer and interlayer exchange interactions can be estimated by the ratio $T_N/\theta_{CW} = (J_\parallel - J_\perp)/(J_\parallel + J_\perp)$ [59,60], showing that $J_\parallel/J_\perp \approx -12.579 < -3/5$. For Mn ions in $MnBi_4Te_7$, the six nearest neighboring in-plane atoms and three nearest neighboring interplane atoms are considered. The spin-flip transition occurs when the field overcomes the antiferromagnetic coupling between the interlayer moments. One can estimate the interlayer molecular field constant as $|\lambda_\perp| = H_c/M_s \sim 15$ [60], where H_c is the critical field at the spin-flip transition and M_s is the saturation magnetization, extrapolated to $T = 0$, as illustrated in Fig. S2.

Figure 1(d) presents the hysteresis loops of isothermal magnetization data $M(H_a)$ showing that the hysteresis gradually disappears with the increasing temperature shown in Fig. S1 of the Supplemental Material [61]. As illustrated in Fig. 1(d), $MnBi_4Te_7$ undergoes a spin-flip transition with hysteresis starting at a field of $H_a^- = 1500$ Oe, in contrast to $MnBi_2Te_4$, which undergoes a spin-flop transition at much higher fields. The low critical field of $MnBi_4Te_7$ again indicates weaker interlayer AFM interactions than in $MnBi_2Te_4$ and the Mn ions of $MnBi_4Te_7$ exhibit much obvious Ising spin characteristic [18,19]. The effective spin Hamiltonian of $MnBi_4Te_7$ can be well described by an Ising model for metamagnet [44,62] based on these phenomena and other related studies [1,10,18,19],

$$\mathscr{H} = -\sum_{ij_\parallel} J_\parallel s_i s_j - \sum_{ij_\perp} J_\perp s_i s_j - H \sum_i s_i, \tag{2}$$

where s denotes the Ising spins defined at each site, $J_\parallel$ describes pairwise nearest-neighbor (NN) interactions within a single triangular layer, and $J_\perp$ corresponds to an NN interlayer coupling, where $J_\parallel > 0$ corresponds to ferromagnetic coupling and $J_\perp < 0$ corresponds to AFM coupling. H refers to uniform magnetic fields. According to the magnetic phase diagram of the model based on mean field theory, there is a tricritical point when competing interaction ratio $\lambda = J_\parallel/J_\perp$ is less than $-3/5$ [44].

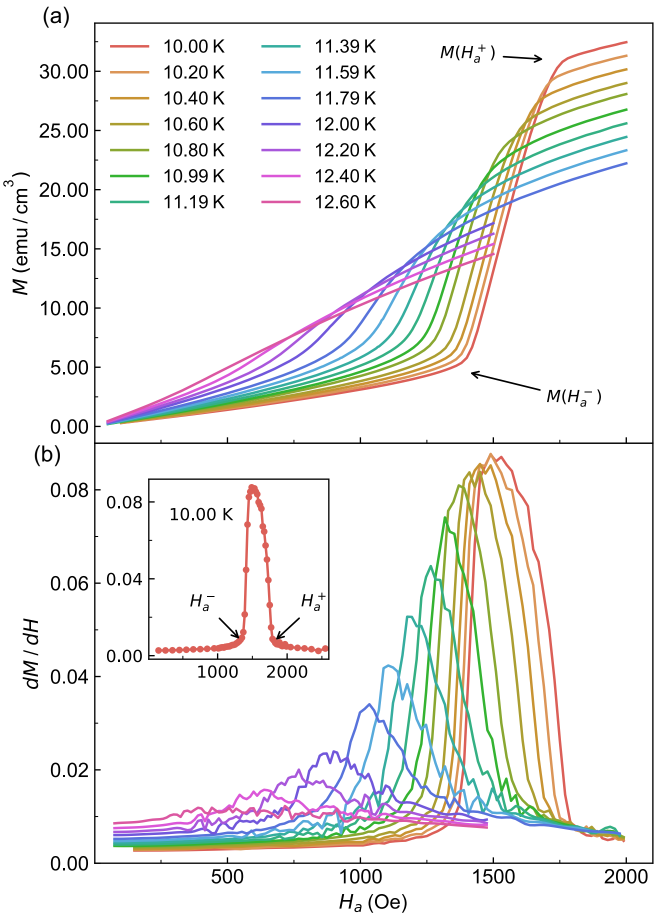

FIG. 2. Typical magnetization data and corresponding susceptibility data of $MnBi_4Te_7$. (a) Magnetization as a function of applied magnetic field at various temperatures approaching the tricritical point. (b) The susceptibility calculated from magnetization (a) as a function of applied magnetic field. The inset shows the typical curve at 10 K. We can define critical fields of the spin-flip transition. H_a^- and H_a^+ are the lower and upper critical fields, respectively.

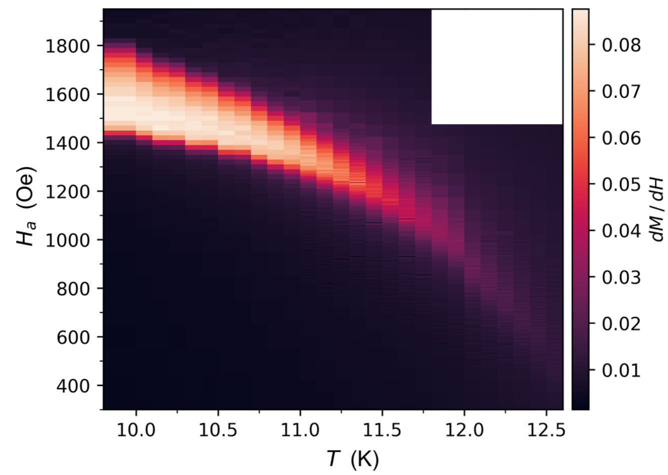

FIG. 3. dM/dH plotted as functions of T and H_a along the c axis of $MnBi_4Te_7$. The mixed phase region gets narrower approaching the TCP.

B. Magnetic phase diagram and tricritical behavior

Typical curves of magnetization and susceptibility as a function of an external magnetic field at different temperatures are shown in Fig. 2. If, at this first-order transition, magnetization M were to increase discontinuously, and be affected in the demagnetizing field shown in Eq. (1), the critical field would decrease to a value below that required to initiate the transition. Therefore, the transition cannot occur all at once, but must proceed gradually under the influence of a demagnetizing field [63,64]. Two degenerate phases and time-reversed antiferromagnetic phases (up-down-up-down $\uparrow\downarrow\uparrow\downarrow$ and down-up-down-up $\downarrow\uparrow\downarrow\uparrow$) exist in the $MnBi_4Te_7$ sample in the absence of magnetic field [65,66]. As the magnetic field increases, a saturated paramagnetic phase is nucleated (usually along the antiferromagnetic wall) at metamagnetic transition resulting in three phases coexisting in the region [66]. The phenomenon means the original first-order transition line splits open to enclose the so called "mixed-phase" region in the magnetic phase diagram as illustrated in Figs. 3, 5, and 6. The upper critical field H_a^+ and lower critical field H_a^- can be determined at temperatures between 10 K and 10.9 K as shown in Fig. 2(a). In the spin flip transition region, the static susceptibility changes sharply and eventually reaches a certain value $dM/dH_a = 1/N$ [63] depicted in the inset of Fig. 2(b) and Fig. S1(b).

However, Eq. (1) applied strictly only for uniform ellipsoids, in that N becomes a function of the magnetic equation of states for all other sample shapes [67]. For our $MnBi_4Te_7$ bulk samples, which cannot be shaped into ellipsoid, the magnetic field tends to be inhomogeneous. The effect for nonellipsoidal samples can be quite significant in regions where dM/dH_i is large, particularly near both first and second order phase transitions. Specifically, as the temperature approaches the tricritical temperature, the slope of magnetization undergoing the first order transition becomes temperature dependent rather than equal to the inverse of the demagnetization factor as shown in Fig. 2(b). These so-called "rounding effects" are very obvious, making it hard to distinguish a small discontinuity just below the tricritical point from a second order inflection just above the tricritical point [68]. Detailed information about the critical internal field, H_i, can be found in Fig. S3 and Fig. S4. The internal field vs temperature phase diagram is shown in Fig. S5 in the Supplemental Material [61]. Some indication of these difficulties is illustrated by $FeCl_2$, one of the two metamagnetic materials on which most of the tricritical point studies have been reported [52–54,69].

To overcome these difficulties, we can measure dynamic magnetization processes. Fortunately, tricritical points involve first order transitions, which are intrinsically susceptible to hysteresis effects and the formation of domains in the regions of coexistence [70]. In single-phase regions, magnetization proceeds via individual spin reversals with single spin-flip time $\tau \sim 10^{-10}$ s. In mixed-phase regions, macroscopic processes involving domains take place. Based on our understanding of such domains [71], with typical spin relaxation time $\tau = (2\pi f)^{-1} \sim 0.1$ s, the low frequency response of the system needs to be measured.

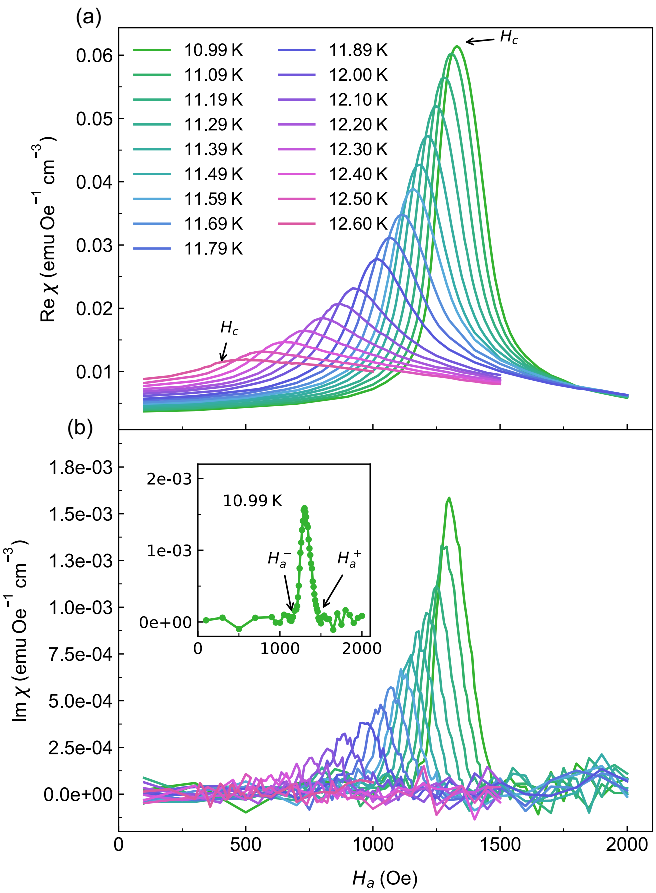

FIG. 4. Typical ac susceptibility data of $MnBi_4Te_7$ as a function of applied magnetic field. Data were recorded for an excitation amplitude of 2 Oe parallel to the c axis at different temperatures. (a) The real part of the ac susceptibility, $\mathrm{Re}\chi_{ac}$, as a function of applied magnetic field for 10 Hz frequency approaching the tricritical temperature. (b) The imaginary part of the ac susceptibility, $\mathrm{Im}\chi_{ac}$, as a function of applied magnetic field. The inset shows the typical curve at 11 K and we define the upper critical fields H_a^+ and lower critical fields H_a^-. We can determine the fields of the second order transition H_c above 12.4 K, where the imaginary part of the susceptibility is approximately equal to zero.

Typical plots of ac susceptibility as a function of applied field are shown in Fig. 4. The real part of the ac susceptibility, $\mathrm{Re}\chi_{ac}$, versus magnetic field at different temperatures are illustrated in Fig. 4(a). $\mathrm{Re}\chi_{ac}$ vs magnetic field for different frequency at 10.99 K are represented in Fig. S9(a) of the Supplemental Material [61]. We are concerned with the mix-phase region, where the quantitative difference between $\mathrm{Re}\chi_{ac}$ is measured at different excitation frequencies due to dynamic effects, as shown in Fig. S9(b).

The imaginary part of the ac susceptibility $\mathrm{Im}\chi_{ac}$ versus magnetic field at different temperatures is shown in Fig. 4(b). $\mathrm{Im}\chi_{ac}$ vs magnetic field plots for different frequencies at 10.99 K and 12.00 K are represented in Figs. S9(c) and S9(d). Similar measurements at different frequencies yield the same locations for the onset of the mixed phase boundaries. The imaginary component, $\mathrm{Im}\chi_{ac}$, indicates dissipative processes in the sample. Relaxation and irreversibility in the mixed phase region give rise to a nonzero $\mathrm{Im}\chi_{ac}$ due to

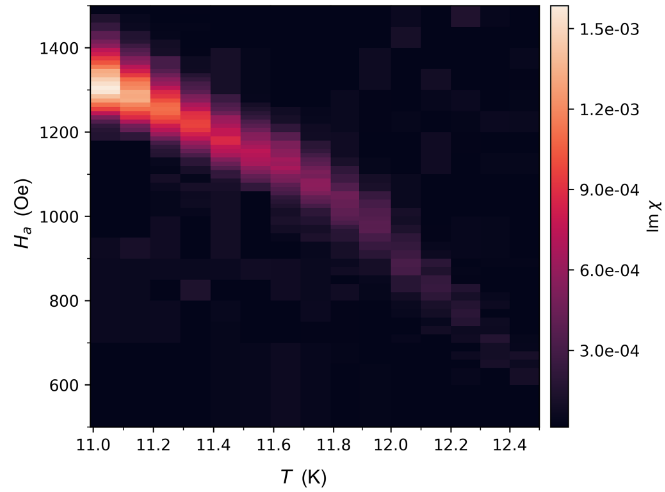

FIG. 5. $\mathrm{Im}\chi_{ac}$ plotted as functions of T and H_a along the c axis of $MnBi_4Te_7$. The mixed phase region gets narrower approaching the TCP.

the irreversible domain wall movement, which was observed in $MnBi_4Te_7$ using cryogenic magnetic force microscopy [66,72]. In our experiments the imaginary component was observable very near the tricritical point, allowing us to map out the phase boundaries below the tricritical temperature. As the temperature increases, the mixed-phase region decreases in size until it ultimately disappears above 12.4 K where $\mathrm{Im}\chi_{ac} \approx 0$, as illustrated in Fig. 4(b). To locate the second-order phase boundary for $T > T_t$, where $\mathrm{Im}\chi_{ac} = 0$, we use the character of the real part of the ac susceptibility. The peaks in the expected region, shown in Fig. 4, served to locate the boundary. The mixed phase narrows as it approaches the TCP as shown in Figs. 3 and 5. The final phase diagram, accurately following the definitions of the characteristic field and temperature values, is illustrated in Fig. 6(a), with the tricritical point identified at (12.4 K, 660 Oe). In the M-T plane the mean-field theory predicts that the two phase lines (SPM and mixed phase, AFM and mixed phase) will approach the tricritical point linearly, with $\beta_2^+ \approx 1$ and $\beta_2^- \approx 1$ [45,73]. The most striking feature of Fig. 6(b) is that these phase boundaries appear to near the TCP linearly, as predicted. Additionally, along the first order line the Landau theory predicts that the discontinuity in the nonordering magnetization should obey the linear law [43], that is, $\Delta M/M_t = A(1 - T/T_t)^{\beta_2}$, compared to our result as shown in the inset of Fig. 6(b), $\beta_2 = 1.02 \pm 0.10$, $A = 21.66 \pm 2.51$, and $T_t = 12.47 \pm 0.04$ K. Note that the fitting data of the reduced temperature ranges from 0.002 to 0.2 and the uncertainties represent statistical errors from the least-squares fit.

The tricritical exponent δ_2 was obtained by a linear least-squares fitting of the log-log normalized magnetization $(M - M_c)/M_c$ against normalized field $(H - H_c)/H_c$, where (H_c, M_c) is the point where susceptibility is at the maximum. A typical plot of $T = 11.79$ K is shown in Fig. 7(a). For both $H > H_c$ and $H < H_c$, the slope of curves near the mix-phase region approaches a limit corresponding to 1. Data away from the mix-phase and critical region tend to approach another limiting slope corresponding to $1/\delta_2 \approx 0.5$ [45,73], dividing

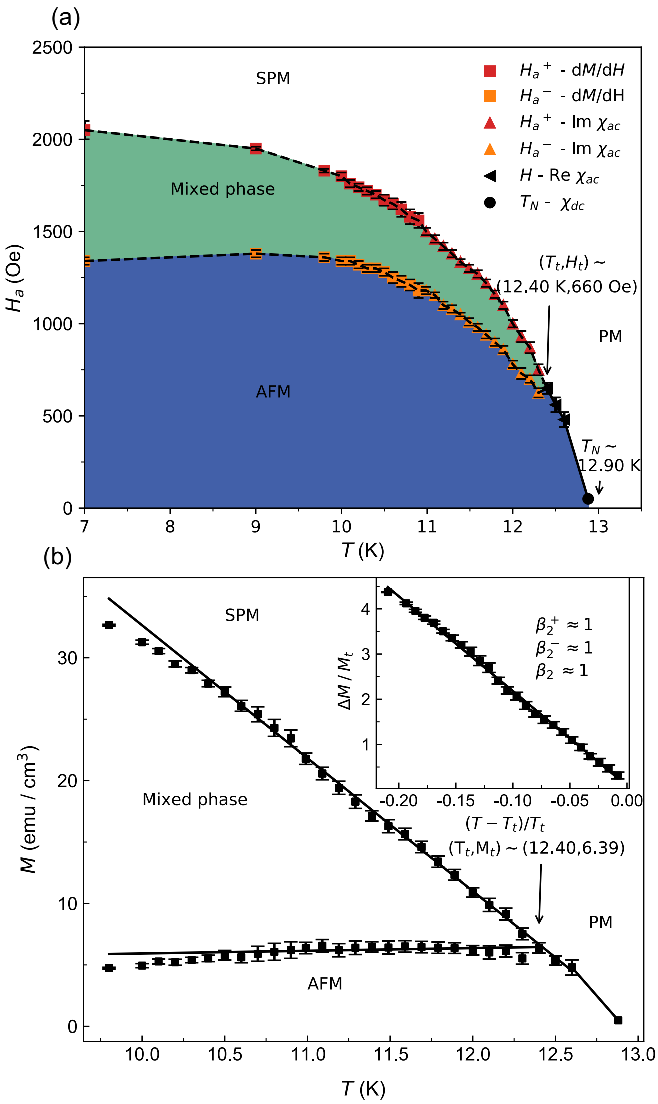

FIG. 6. (a) Magnetic phase diagram of $MnBi_4Te_7$ as a function applied magnetic field and temperature along the c axis. The tricritical point (T_t, H_t) for our measurement accuracy is (12.40 K, 660 Oe) and the Néel temperature is about 12.9 K. (b) M-T phase diagram. M_t is tricritical magnetization, $M_t = 6.39 \pm 0.43$ emu/cm^3. The magnetization values plotted in the diagram correspond to the values under H_a^+ or H_a^- critical fields and the error bars reflect the uncertainty in locating the onset of the susceptibilities. The exponents β_2^+, β_2^- mean normalized magnetization change along different paths, upper boundary H^+ and lower boundary H^- of mixed phase, respectively. We can define β_2 according to $\Delta M/M_t \sim (1 - T/T_t)^{\beta_2}$, where $\Delta M = M(H_a^+) - M(H_a^-)$. The inset shows data for the discontinuity close to the TCP.

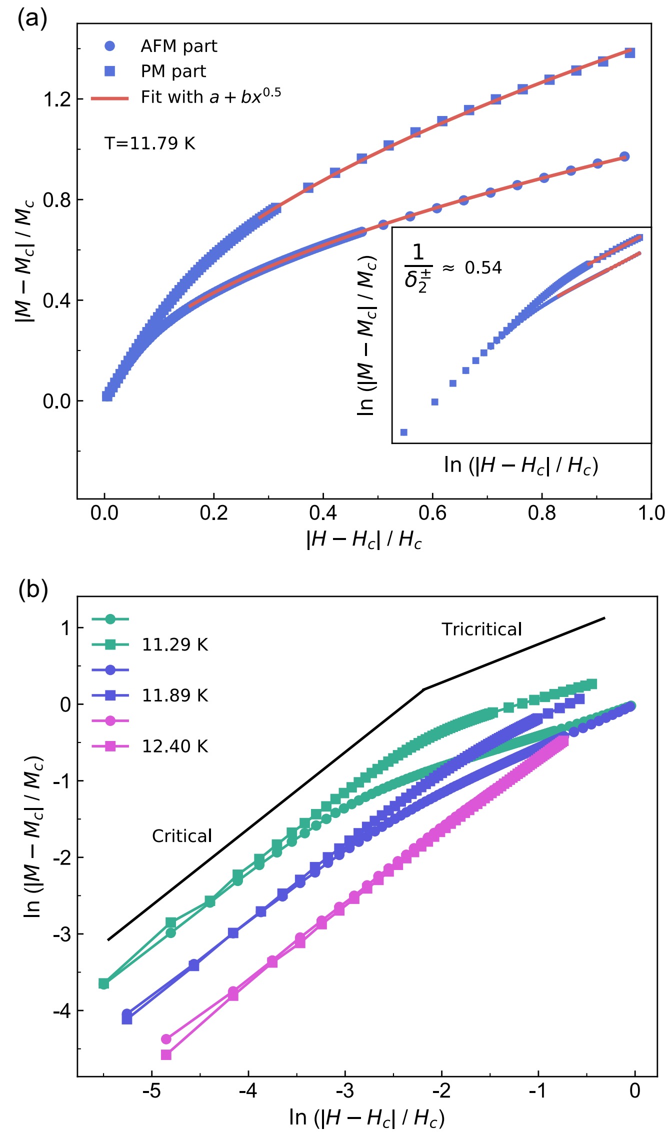

FIG. 7. Tricritical exponent δ_2 can be defined by $M \sim H^{1/\delta_2}$ approaching TCP. (a) Typical normalized magnetization versus normalized field at 11.79 K. The inset shows double logarithmic plots for both the paramagnetic part $H > H_c$ and antiferromagnetic part $H < H_c$. The red line is fitted with the tricritical relation, $M \sim H^{1/2}$, and we can determine tricritical region data. (b) Double logarithmic plots of normalized magnetization and normalized field for different isotherms. Lines have slopes 0.95 ± 0.02 (critical) and 0.52 ± 0.09 (tricritical) corresponding to $1/\delta_2 = 0.52 \pm 0.09$. The crossover from critical to tricritical regime is controlled by the crossover exponent $\Phi_2 = \delta_2\beta_2$.

into two distinct parts corresponding to antiferromagnetic and paramagnetic phases as shown in Fig. 7(b). The separation of two parts disappears as the temperature approaches $T_t = 12.4$ K. These crossover effects arise from competition between the second-order and tricritical phase transition for multicomponent systems [39].

Finally, we tested the tricritical scaling hypothesis discussed in the Appendix using data from eight isotherms below T_t. Figure 8 shows scaling plots for the isothermal magnetization, $m/|t|^{\beta_2}$ vs $h_2/|t|^{\beta_2\delta_2}$, where $h_2 = h + pt$, $t = (T - T_t)/T_t$, $m = (M - M_t)/M_t$, and $h = (H - H_t)/H_t$; (H_t, T_t) is the TCP, M_t is the tricritical magnetization, and p is the slope of the phase boundary at the TCP in $h - t$ space. Values for $T_t = 12.40$ K, $H_t = 660$ Oe, and $M_t = 6.39$ emu/cm^3 were taken from Fig. 6, and $p = -12.18 \pm 3.52$ was derived from Figs. 6(a) and S6 [61]. Using the theoretically predicted exponents $\beta_2 = 1$ and $\delta_2 = 2$, the data failed to collapse onto a single curve, violating the scaling hypothesis illustrated in Fig. 8(a). By varying those exponents β_2 and δ_2, however,

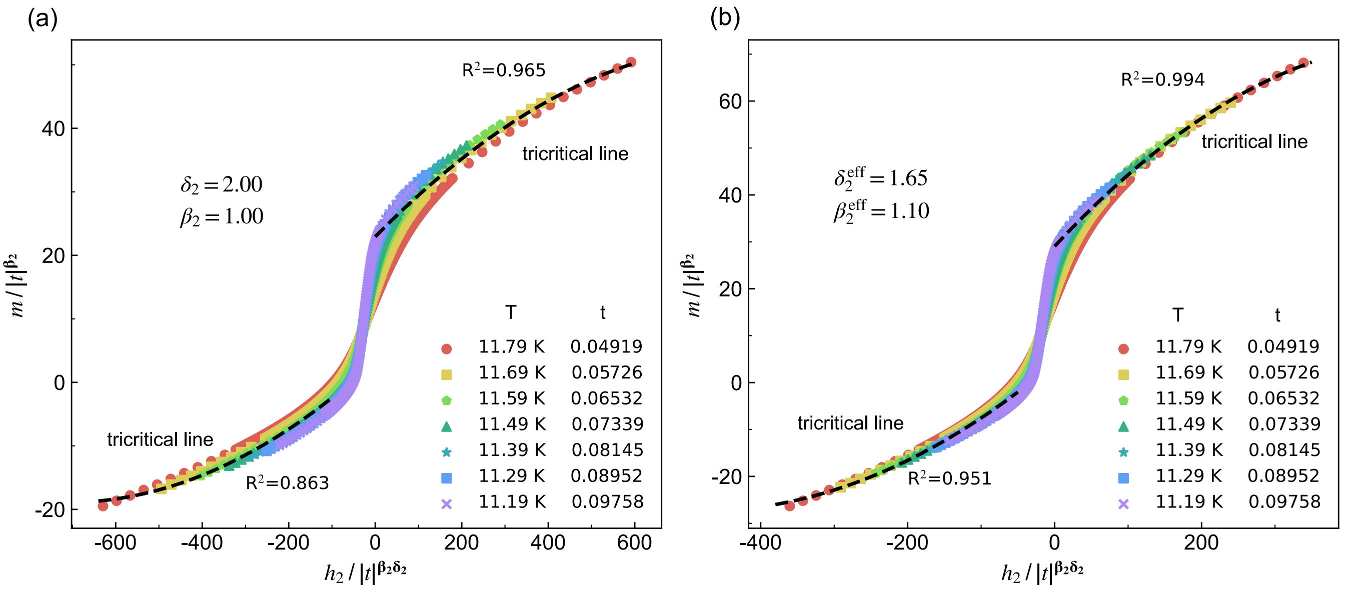

FIG. 8. (a) Scaling plot of $m/|t|^{\beta_2}$ versus $h_2/|t|^{\beta_2\delta_2}$ [Eq. (A19)] using mean-field exponents. (b) Scaling magnetization data vs scaling variable with the effective tricritical exponents $\beta_2^{\rm eff} = 1.10$ and $\delta_2^{\rm eff} = 1.65$. Using Eq. (A22), the dotted line is fitted to the data from the tricritical region as in Fig. 7.

good data collapsing can be obtained with effective values $\delta_2^{\rm eff} = 1.65$, $\beta_2^{\rm eff} = 1.10$ as shown in Fig. 8(b). The equation (A24) where the mean-field power law is corrected by the logarithmic factor $|\ln|t||^{1/2}$ and the results are presented in Figs. 9 and S8 [61]. The tricritical region data were fitted using each of the relations presented in Figs. 8 and 9 and the results of the analysis are quantitatively illustrated in Table S1. This table includes the R-squared, a goodness-of-fit measure for regression models, and the best-fit coefficients. The fit to the mean-field theory relation, $\beta_2 = 1$, $\delta_2 = 2$, and Eq. (A22), resulted in coefficients yielding a value of $R^2 = 0.965, 0.863$, which is relatively deviated from 1. The mean-field theory

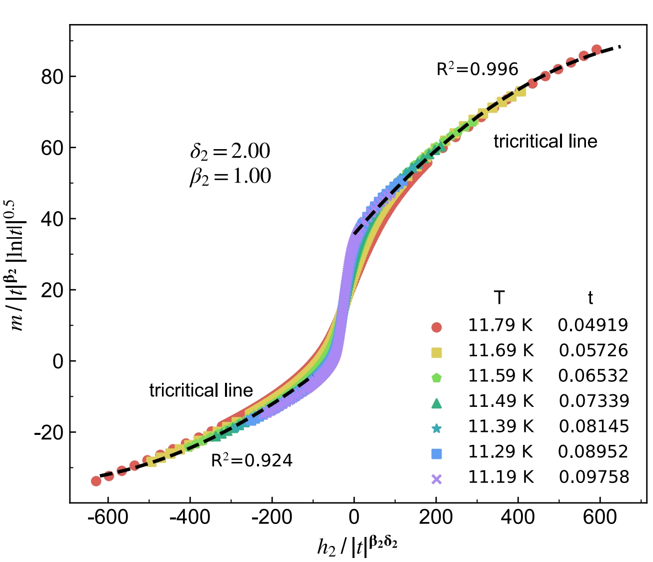

FIG. 9. Data of Fig. 8 scaled according to $m/|t|^{\beta_2}|\ln|t||^{0.5}$ vs $h_2/|t|^{\beta_2\delta_2}$ with mean-field exponents $\delta_2 = 2$, $\beta_2 = 1$ and logarithmic correction. The dotted line is fitted to the tricritical data with Eq. (A24).

relation is ruled out as would be expected. The fits with effective exponents $\beta_2^{\rm eff} = 1.10$, $\delta_2^{\rm eff} = 1.65$ and the mean-field exponents with logarithmic correction obtained $R^2 = 0.994, 0.951$ and $R^2 = 0.996, 0.924$, respectively, which are summarized in Table S1. Our fits indicate that the effective power law and predicted logarithmic corrections to a mean-field theory power law are similar within our experimental accuracy. However, crystallographic defects such as vacancy, site mixing, and mismatch of layers have been reported for the family of compounds [13,20,74]. The size of the region perturbed by the defect increases near T_t because the nonordering parameter, magnetization, changes in the vicinity of the defect. The structure of the substance near T_t becomes "soft" [75] (those modes in which the eigenfrequency tends to 0) with respect to the changes of magnetization. In particular, the characteristic correlation length $r_c \sim (1 - T/T_t)^{-\nu}$ for spatial changes of the magnetization fixed at a given point (in this case on the defect) becomes infinite as $(1 - T/T_t) \to 0$ [75]. Increasing the dimensions of the region (line defects or surface defects) leads to an increase of the cross section for domain formation (where the magnetic moment is polarized) and therefore an increase of magnetization due to fluctuations in the defect concentration. For the metamagnetic transition especially near the tricritical point, the saturated paramagnetic phase with large magnetization nucleates along the antiferromagnetic walls (usually caused by mismatch of layers) or at the point defect (vacancy and site mixing). Such defects cause the power law to deviate from the tricritical scaling law near the tricritical point, preventing the data in Figs. 8(b) and 9 from collapsing completely into a single curve.

Actually, for the tricritical point, Ridel and Wegner *et al.* employed the renormalization method to obtain mean-field exponents and subsequently extended the treatment to include logarithmic corrections to mean-field behavior at a borderline lattice dimension $d^+ = 3$ [76,77]. While mean-field theory does not account for fluctuations, near the tricritical point, these fluctuations cannot be ignored. The logarithmic corrections essentially come from the contributions of nonnegligible fluctuation. However, Shang and Salamon found, in $FeCl_2$ systems, the fact that the logarithmic correction mimics a small fractional power law over a restricted range of data, which makes it difficult to detect the logarithmic correction unambiguously [55]. They also obtained effective tricritical exponents that deviated from the mean-field theory prediction. Therefore, the difference between these exponents and the mean-field exponents comes from the logarithmic correction. We have tabulated the tricritical exponents for $MnBi_4Te_7$ in Table I, along with values for tricritical systems. In the future, the contribution of massless Dirac fermions to the tricritical exponent in the few layers of $MnBi_4Te_7$ should be investigated, which potentially may lead to the discovery of new classes of universality, such as chiral Ising or tricritical universality [29–31]. The properties of supersymmetry can emerge at the quantum tricritical point of a topological phase [32–34]. However, there are Mn vacancies and extra Bi on the Mn site in the as-grown MnBiTe family, which makes the Fermi level E_F of $MnBi_4Te_7$ below the Dirac point [13], but we can tune its chemical potential by substituting the Sb element for Bi in $MnBi_4Te_7$ [78].

IV. CONCLUSION

In summary, we have studied the tricritical phenomena of intrinsic magnetic topological insulator $MnBi_4Te_7$. We found that the magnetic phase diagram of $MnBi_4Te_7$ has a tricritical point as a layered metamagnet. Based on the tricritical scaling theory, we obtain the effective tricritical exponents $\beta_2^{\text{eff}} \sim 1.10$ and $\delta_2^{\text{eff}} \sim 1.65$, which are different from the mean-field values and result from the logarithmic correction $|\ln|t||^{0.5}$. The scaling plots using these exponents show that the tricritical hypothesis is correct for our sample $MnBi_4Te_7$. Importantly, the topological metamagnet $MnBi_4Te_7$ provides a suitable platform to further study tricriticality and topological transition due to the competitive interactions and the nontrivial band structure.

ACKNOWLEDGMENTS

This work was supported by the National Key R&D Program of China (Grant No. 2022YFA1203903) and the National Natural Science Foundation of China (Grants No. 52071324, No. 52271192, and No. 52031014). We gratefully acknowledge W. Ren for his helpful guidance of the single crystal grown.

APPENDIX A: TRICRITICAL SCALING THEORY

A complete description of asymptotic tricriticality for a metamagnet, developed by Riedel [39], and Griffiths [79], requires consideration of the temperature, T, the uniform magnetic field, $H_2 = H$, and the staggered field, H_1. The phase diagram in the symmetry plane means $H_1 = 0$. It is appropriate to introduce suitable scaling fields, $t = (T - T_t)/T_t$, $h_2 = (H_2 - H_{2t})/H_{2t} + pt$, and $h_1 = H_1$, where axis t is tangent to the phase boundary at TCP with slope p as shown in Fig. 10. The tricritical scaling hypothesis [80,81] can be formulated in terms of the scaling fields t and h_2: asymptotically close to the tricritical point we can assume the singular part of the Gibbs potential, $G_{\text{sing}}(t, h_1, h_2)$,

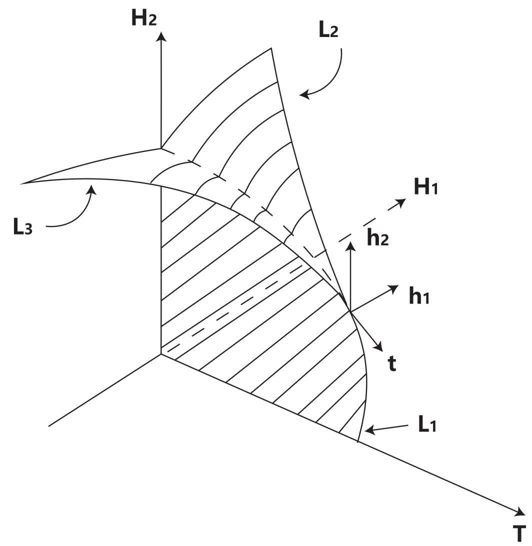

FIG. 10. Tricritical phase diagram of a metamagnet in the space of temperature T, staggered magnetic field H_1, and uniform magnetic field H_2. The tricritical point is (T_t, H_{2t}) [43].

$$G_{\text{sing}}(t, h_1, h_2) \approx |t|^{2-\alpha}\mathscr{G}^{(\pm)}\left(\frac{h_1}{|t|^{\phi_1}}, \frac{h_2}{|t|^{\phi_2}}\right), \tag{A1}$$

where the thermal exponent α and the crossover exponent ϕ_2 are associated specifically with the tricritical point, and the superscript $(\pm)$ represents the sign of t.

Leading behavior along the H_2 axis in the plane of symmetry is

$$G_{\text{sing}}(t, h_1, h_2) \approx |h_2|^{2-\alpha_t}\mathscr{G}^{(\pm)}\left(\frac{h_1}{|h_2|^{\phi_{1t}}}, \frac{t}{|h_2|^{\phi_{2t}}}\right). \tag{A2}$$

The scaling and analytic properties of the Gibbs potential are, of course, inherited by its various derivatives which are the physical observables.

Therefore, we can define the nonordering magnetization (uniform magnetization) $m_2 = M$ and order magnetization (staggered magnetization) m_1,

$$m_1(T, H_1, H_2) = -\left(\frac{\partial G}{\partial H_1}\right)_{T,H_2}, \tag{A3a}$$

$$m_2(T, H_1, H_2) = -\left(\frac{\partial G}{\partial H_2}\right)_{T,H_1}, \tag{A3b}$$

and the scaling hypothesis implies that

$$m_1(t, h_1, h_2) \approx |t|^{\beta_1}\mathscr{M}_1^{(\pm)}\left(\frac{h_1}{|t|^{\phi_1}}, \frac{h_2}{|t|^{\phi_2}}\right), \tag{A4a}$$

$$m_2(t, h_1, h_2) \approx |t|^{\beta_2}\mathscr{M}_2^{(\pm)}\left(\frac{h_1}{|t|^{\phi_1}}, \frac{h_2}{|t|^{\phi_2}}\right). \tag{A4b}$$

The new tricritical exponent, β_i, is given by

$$\beta_i = 2 - \alpha - \phi_i, \quad i = 1, 2. \tag{A5}$$

In a similar way, one can define the corresponding susceptibilities by

$$\chi_1(t,H_1,H_2)=\left(\frac{\partial m_1}{\partial H_1}\right)_{t,H_2}, \tag{A6a}$$

$$\chi_2(t,H_1,H_2)=\left(\frac{\partial m_2}{\partial H_2}\right)_{t,H_1} \tag{A6b}$$

and we have

$$\chi_1(t,h_1,h_2)\approx|t|^{-\gamma_1}\mathscr{X}_1^{(\pm)}\left(\frac{h_1}{|t|^{\phi_1}},\frac{h_2}{|t|^{\phi_2}}\right), \tag{A7a}$$

$$\chi_2(t,h_1,h_2)\approx|t|^{-\gamma_2}\mathscr{X}_2^{(\pm)}\left(\frac{h_1}{|t|^{\phi_1}},\frac{h_2}{|t|^{\phi_2}}\right), \tag{A7b}$$

$$\gamma_i=-(2-\alpha-2\phi_i),\quad i=1,2, \tag{A8}$$

where $\mathscr{M}_i$ and $\mathscr{X}_i$ are the new scaling functions. The behavior of the moment m_2 and the susceptibilities, χ_2, along the various paths approach the tricritical point in the space (t,h_2).

We can also discuss the leading behavior along the H_2 axis, in which it might be convenient to use the scaling assumption in the form (A2). One can rewrite those observables as

$$m_1(t,h_1,h_2)\approx|h_2|^{\beta_{1t}}\mathscr{M}_{1t}^{(\pm)}\left(\frac{h_1}{|h_2|^{\phi_{1t}}},\frac{t}{|h_2|^{\phi_{2t}}}\right), \tag{A9a}$$

$$m_2(t,h_1,h_2)\approx|h_2|^{\beta_{2t}}\mathscr{M}_{2t}^{(\pm)}\left(\frac{h_1}{|h_2|^{\phi_{1t}}},\frac{t}{|h_2|^{\phi_{2t}}}\right) \tag{A9b}$$

and

$$\chi_1(t,h_1,h_2)\approx|h_2|^{-\gamma_{1t}}\mathscr{X}_{1t}^{(\pm)}\left(\frac{h_1}{|h_2|^{\phi_{1t}}},\frac{t}{|h_2|^{\phi_{2t}}}\right), \tag{A10a}$$

$$\chi_2(t,h_1,h_2)\approx|h_2|^{-\gamma_{2t}}\mathscr{X}_{2t}^{(\pm)}\left(\frac{h_1}{|h_2|^{\phi_{1t}}},\frac{t}{|h_2|^{\phi_{2t}}}\right), \tag{A10b}$$

where the corresponding tricritical exponents obey

$$\beta_{1t}=2-\alpha_t-\phi_{1t}=\beta_1/\phi_2=1/\delta_{12}, \tag{A11a}$$

$$\beta_{2t}=1-\alpha_t=\beta_2/\phi_2=1/\delta_2 \tag{A11b}$$

and

$$\gamma_{1t}=-(2-\alpha_t-2\phi_{1t})=\gamma_1/\phi_2, \tag{A12a}$$

$$\gamma_{2t}=\alpha_t=\gamma_2/\phi_2. \tag{A12b}$$

Based on the above relations one finds

$$m_1(t,h_1,h_2)\sim|h_2|^{1/\delta_{12}}, \tag{A13a}$$

$$m_2(t,h_1,h_2)\sim|h_2|^{1/\delta_2}, \tag{A13b}$$

where

$$1/\delta_{12}=\beta_1/\phi_2, \tag{A14a}$$

$$1/\delta_2=\beta_2/\phi_2. \tag{A14b}$$

The tricritical exponents satisfy the Fisher-Essam relation [82,83] and the Widom relation [84]:

$$\alpha+2\beta_2+\gamma_2=2, \tag{A15}$$

$$\gamma_2=\beta_2(\delta_2-1). \tag{A16}$$

The exponents with subscript t are the tricritical exponents in the notation of Griffiths [79] and they satisfy the relations as the above set of exponents

$$\alpha_t+2\beta_{it}+\gamma_{it}=2,\quad i=1,2, \tag{A17}$$

$$\gamma_{it}=\beta_{it}(\delta_{i2}-1),\quad i=1,2, \tag{A18}$$

where $\delta_{22}=\delta_2$. The exponents can be subdivided into two classes: (i) the exponents defined with subscript t by regarding the tricritical point as a particular point on the line of critical points, α_t, β_{it}, γ_{it}, and (ii) describing the tricritical behavior in analogy with an "ordinary" critical point, α, β_i, γ_i. It is apparent from Fig. 10 that the set of exponents (ii) describes the tricritical behavior along the path tangentially to the phase boundary in the symmetry plane, whereas the set of exponents (i) characterizes the singular behavior along a path approaching the tricritical point at a finite angle with the phase boundary. Both sets of exponents are related through the crossover exponent ϕ_2. The exponents discussed in this article are predicted to have mean-field values, $\beta_2=1$, $\gamma_2=1$, $\delta_2=2$.

The tricritical scaling hypothesis makes specific predictions concerning the form of the nonordering magnetic equation of state discussed in Eq. (A4). We begin by rewriting the nonorder magnetic equation of state in the form

$$m_2(t,h_1,h_2)\approx|t|^{\beta_2}\mathscr{M}_2^{(\pm)}\left(\frac{h_1}{|t|^{\phi_1}},\frac{h_2}{|t|^{\phi_2}}\right)$$

using the scaling parameters in favor of the tricritical exponents $\phi_2=\beta_2\delta_2$, $h_1=0$ and the above equation becomes

$$m_2(t,h_2)/|t|^{\beta_2}\approx\mathscr{M}_2^{(\pm)}\left(\frac{h_2}{|t|^{\beta_2\delta_2}}\right). \tag{A19}$$

Next we can define the variables

$$\mathscr{m}\equiv|t|^{-\beta_2}m_2(t,h_2), \tag{A20a}$$

$$\mathscr{h}\equiv|t|^{-\beta_2\delta_2}h_2(t,m_2). \tag{A20b}$$

Hence Eq. (A20) can be written in terms of the reduced variables as

$$\mathscr{m}=F_\pm(\mathscr{h}), \tag{A21a}$$

$$\mathscr{h}=f_\pm(\mathscr{m}), \tag{A21b}$$

where the scaled function $f_\pm(\mathscr{m})$ is the inverse of the scaled function $F_\pm(\mathscr{h})$. Equations (A20) and (A21) predict that the plots $\mathscr{m}$ vs $\mathscr{h}$ should fall on a universal curve for the tricritical data.

For Fig. 8, one might expect $F_{\pm}(\hbar)$ is in the form

$$\mathscr{m} = F_{\pm}(\hbar) = a_0 + a_1\hbar + a_2\hbar^2 + \cdots, \tag{A22}$$

In Fig. 9 the scaled magnetization is compared to the logarithmic correction factor $|\ln|t||^{0.5}$ and it can be described by the relation

$$m_2(t, h_2)/|t|^{\beta_2}|\ln|t||^{0.5} \approx \mathscr{M}_2^{(\pm)}\left(\frac{h_2}{|t|^{\phi_2}}\right). \tag{A23}$$

It is quite common to define Eqs. (A20)–(A22) in the equivalent form

$$\mathscr{m}' \equiv |t|^{-\beta_2} m_2(t, h_2)|\ln|t||^{0.5}, \tag{A24a}$$

$$\mathscr{m}' = F'_{\pm}(\hbar'), \tag{A24b}$$

$$\hbar' = f'_{\pm}(\mathscr{m}'), \tag{A24c}$$

$$\mathscr{m}' = F_{\pm}(\hbar') = a_0 + a_1\hbar' + a_2\hbar'^2 + \cdots. \tag{A24d}$$

[1] M. M. Otrokov, I. I. Klimovskikh, H. Bentmann, D. Estyunin, A. Zeugner, Z. S. Aliev, S. Gaß, A. Wolter, A. Koroleva, A. M. Shikin *et al.*, Prediction and observation of an antiferromagnetic topological insulator, Nature (London) **576**, 416 (2019).

[2] H. Sun, B. Xia, Z. Chen, Y. Zhang, P. Liu, Q. Yao, H. Tang, Y. Zhao, H. Xu, and Q. Liu, Rational design principles of the quantum anomalous Hall effect in superlatticelike magnetic topological insulators, Phys. Rev. Lett. **123**, 096401 (2019).

[3] Y. Hu, L. Xu, M. Shi, A. Luo, S. Peng, Z. Y. Wang, J. J. Ying, T. Wu, Z. K. Liu, C. F. Zhang, Y. L. Chen, G. Xu, X.-H. Chen, and J.-F. He, Universal gapless dirac cone and tunable topological states in $(MnBi_2Te_4)_m(Bi_2Te_3)_n$ heterostructures, Phys. Rev. B **101**, 161113(R) (2020).

[4] K. He, $MnBi_2Te_4$-family intrinsic magnetic topological materials, npj Quantum Mater. **5**, 90 (2020).

[5] Y. Gong, J. Guo, J. Li, K. Zhu, M. Liao, X. Liu, Q. Zhang, L. Gu, L. Tang, X. Feng, D. Zhang *et al.*, Experimental realization of an intrinsic magnetic topological insulator, Chin. Phys. Lett. **36**, 076801 (2019).

[6] X. Wu, J. Li, X. M. Ma, Y. Zhang, Y. Liu, C.-S. Zhou, J. Shao, Q. Wang, Y.-J. Hao, Y. Feng *et al.*, Distinct topological surface states on the two terminations of $MnBi_4Te_7$, Phys. Rev. X **10**, 031013 (2020).

[7] P. Swatek, Y. Wu, L.-L. Wang, K. Lee, B. Schrunk, J. Yan, and A. Kaminski, Gapless Dirac surface states in the antiferromagnetic topological insulator $MnBi_2Te_4$, Phys. Rev. B **101**, 161109(R) (2020).

[8] H. Deng, Z. Chen, A. Wołoś, M. Konczykowski, K. Sobczak, J. Sitnicka, I. V. Fedorchenko, J. Borysiuk, T. Heider, Ł. Pluciński *et al.*, High-temperature quantum anomalous Hall regime in a $MnBi_2Te_4/Bi_2Te_3$ superlattice, Nat. Phys. **17**, 36 (2021).

[9] E. D. L. Rienks, S. Wimmer, J. Sánchez-Barriga, O. Caha, P. S. Mandal, J. Růžička, A. Ney, H. Steiner, V. V. Volobuev, H. Groiss, M. Albu, G. Kothleitner *et al.*, Large magnetic gap at the dirac point in $Bi_2Te_3/MnBi_2Te_4$ heterostructures, Nature (London) **576**, 423 (2019).

[10] C. Hu, K. N. Gordon, P. Liu, J. Liu, X. Zhou, P. Hao, D. Narayan, E. Emmanouilidou, H. Sun, Y. Liu *et al.*, A van der Waals antiferromagnetic topological insulator with weak interlayer magnetic coupling, Nat. Commun. **11**, 97 (2020).

[11] H.-K. Xu, M. Gu, F. Fei, Y.-S. Gu, D. Liu, Q.-Y. Yu, S.-S. Xue, X.-H. Ning, B. Chen, H. Xie, Z. Zhu, D. Guan, S. Wang, Y. Li, C. Liu, Q. Liu, F. Song, H. Zheng, and J. Jia, Observation of magnetism-induced topological edge state in antiferromagnetic topological insulator $MnBi_4Te_7$, ACS Nano **16**, 9810 (2022).

[12] D. Ovchinnikov, J. Cai, Z. Lin, Z. Fei, Z. Liu, Y.-T. Cui, D. H. Cobden, J.-H. Chu, C.-Z. Chang, D. Xiao *et al.*, Topological current divider in a chern insulator junction, Nat. Commun. **13**, 5967 (2022).

[13] R. C. Vidal, A. Zeugner, J. I. Facio, R. Ray, M. H. Haghighi, A. U. B. Wolter, L. T. Corredor Bohorquez, F. Caglieris, S. Moser, T. Figgemeier *et al.*, Topological electronic structure and intrinsic magnetization in $MnBi_4Te_7$: a Bi_2Te_3 derivative with a periodic Mn sublattice, Phys. Rev. X **9**, 041065 (2019).

[14] Y. J. Chen, L. X. Xu, J. H. Li, Y. W. Li, H. Y. Wang, C. F. Zhang, H. Li, Y. Wu, A. J. Liang, C. Chen *et al.*, Topological electronic structure and its temperature evolution in antiferromagnetic topological insulator $MnBi_2Te_4$, Phys. Rev. X **9**, 041040 (2019).

[15] M. M. Otrokov, I. P. Rusinov, M. Blanco-Rey, M. Hoffmann, A. Y. Vyazovskaya, S. V. Eremeev, A. Ernst, P. M. Echenique, A. Arnau, and E. V. Chulkov, Unique thickness-dependent properties of the van der Waals interlayer antiferromagnet $MnBi_2Te_4$ films, Phys. Rev. Lett. **122**, 107202 (2019).

[16] Y. Deng, Y. Yu, M. Z. Shi, Z. Guo, Z. Xu, J. Wang, X. H. Chen, and Y. Zhang, Quantum anomalous Hall effect in intrinsic magnetic topological insulator $MnBi_2Te_4$, Science **367**, 895 (2020).

[17] C. Liu, Y. Wang, H. Li, Y. Wu, Y. Li, J. Li, K. He, Y. Xu, J. Zhang, and Y. Wang, Robust axion insulator and chern insulator phases in a two-dimensional antiferromagnetic topological insulator, Nat. Mater. **19**, 522 (2020).

[18] B. Li, J.-Q. Yan, D. M. Pajerowski, E. Gordon, A.-M. Nedić, Y. Sizyuk, L. Ke, P. P. Orth, D. Vaknin, and R. J. McQueeney, Competing magnetic interactions in the antiferromagnetic topological insulator $MnBi_2Te_4$, Phys. Rev. Lett. **124**, 167204 (2020).

[19] A. Tan, V. Labracherie, N. Kunchur, A. U. B. Wolter, J. Cornejo, J. Dufouleur, B. Büchner, A. Isaeva, and R. Giraud, Metamagnetism of weakly coupled antiferromagnetic topological insulators, Phys. Rev. Lett. **124**, 197201 (2020).

[20] L. Ding, C. Hu, F. Ye, E. Feng, N. Ni, and H. Cao, Crystal and magnetic structures of magnetic topological insulators $MnBi_2Te_4$ and $MnBi_4Te_7$, Phys. Rev. B **101**, 020412(R) (2020).

[21] M. Z. Hasan and C. L. Kane, Colloquium: Topological insulators, Rev. Mod. Phys. **82**, 3045 (2010).

[22] X.-L. Qi and S.-C. Zhang, Topological insulators and superconductors, Rev. Mod. Phys. **83**, 1057 (2011).

[23] R. Yu, W. Zhang, H.-J. Zhang, S.-C. Zhang, X. Dai, and Z. Fang, Quantized anomalous Hall effect in magnetic topological insulators, Science **329**, 61 (2010).

[24] K. Yasuda, M. Mogi, R. Yoshimi, A. Tsukazaki, K. S. Takahashi, M. Kawasaki, F. Kagawa, and Y. Tokura, Quantized chiral edge conduction on domain walls of a magnetic topological insulator, Science **358**, 1311 (2017).

[25] M. Allen, Y. Cui, E. Y. Ma, M. Mogi, M. Kawamura, I. C. Fulga, D. Goldhaber-Gordon, Y. Tokura, and Z.-X. Shen, Visualization of an axion insulating state at the transition between 2 chiral quantum anomalous Hall states, Proc. Natl. Acad. Sci. USA **116**, 14511 (2019).

[26] C.-Z. Chang, C.-X. Liu, and A. H. MacDonald, Colloquium: quantum anomalous Hall effect, Rev. Mod. Phys. **95**, 011002 (2023).

[27] W. D. Metz, Phase changes: A universal theory of critical phenomena, Science **181**, 147 (1973).

[28] P. M. A. Mestrom, V. E. Colussi, T. Secker, G. P. Groeneveld, and S. J. J. M. F. Kokkelmans, van der Waals universality near a quantum tricritical point, Phys. Rev. Lett. **124**, 143401 (2020).

[29] B. Rosenstein, H.-L. Yu, and A. Kovner, Critical exponents of new universality classes, Phys. Lett. B **314**, 381 (1993).

[30] L. N. Mihaila, N. Zerf, B. Ihrig, I. F. Herbut, and M. M. Scherer, Gross-Neveu-Yukawa model at three loops and Ising critical behavior of Dirac systems, Phys. Rev. B **96**, 165133 (2017).

[31] S. Yin, S.-K. Jian, and H. Yao, Chiral tricritical point: A new universality class in Dirac systems, Phys. Rev. Lett. **120**, 215702 (2018).

[32] S.-K. Jian, C.-H. Lin, J. Maciejko, and H. Yao, Emergence of supersymmetric quantum electrodynamics, Phys. Rev. Lett. **118**, 166802 (2017).

[33] T. Grover, D. N. Sheng, and A. Vishwanath, Emergent spacetime supersymmetry at the boundary of a topological phase, Science **344**, 280 (2014).

[34] E. O'Brien and P. Fendley, Lattice supersymmetry and order-disorder coexistence in the tricritical Ising model, Phys. Rev. Lett. **120**, 206403 (2018).

[35] Z. D. Zhang, Conjectures on the exact solution of three-dimensional (3D) simple orthorhombic Ising lattices, Philos. Mag. **87**, 5309 (2007).

[36] H. E. Stanley, *Phase Transitions and Critical Phenomena* (Clarendon Press, Oxford, 1971), Vol. 7.

[37] F. Gao, J. Huang, W. Ren, M. Li, H. Wang, T. Yang, B. Li, and Z. Zhang, Magnetic and transport properties of the topological compound DySbTe, Phys. Rev. B **105**, 214434 (2022).

[38] W. Liu, D. Liang, F. Meng, J. Zhao, W. Zhu, J. Fan, L. Pi, C. Zhang, L. Zhang, and Y. Zhang, Field-induced tricritical phenomenon and multiple phases in DySb, Phys. Rev. B **102**, 174417 (2020).

[39] E. K. Riedel, Scaling approach to tricritical phase transitions, Phys. Rev. Lett. **28**, 675 (1972).

[40] L. D. Landau, *Course of Theoretical Physics* (Pergamon Press, New York, 1958), Vol. 5.

[41] R. B. Griffiths, Thermodynamics near the two-fluid critical mixing point in He^3-He^4, Phys. Rev. Lett. **24**, 715 (1970).

[42] E. Stryjewski and N. Giordano, Metamagnetism, Adv. Phys. **26**, 487 (1977).

[43] C. Domb, *Phase Transitions and Critical Phenomena* (Elsevier, Amsterdam, 2000), Vol. 9.

[44] J. M. Kincaid and E. G. D. Cohen, Phase diagrams of liquid helium mixtures and metamagnets: experiment and mean field theory, Phys. Rep. **22**, 57 (1975).

[45] R. Bausch, Ginzburg criterion for tricritical points, Z. Phys. **254**, 81 (1972).

[46] J. A. Griffin, J. D. Litster, and A. Linz, Spontaneous magnetization at marginal dimensionality in $LiTbF_4$, Phys. Rev. Lett. **38**, 251 (1977).

[47] K. G. Wilson and J. Kogut, The renormalization group and the ϵ expansion, Phys. Rep. **12**, 75 (1974).

[48] F. J. Wegner, Corrections to scaling laws, Phys. Rev. B **5**, 4529 (1972).

[49] N. Giordano and W. P. Wolf, Experimental study of the tricritical "wings" in dysprosium aluminum garnet, Phys. Rev. Lett. **39**, 342 (1977).

[50] N. Giordano and W. Wolf, New method for investigating magnetic tricritical points, Phys. Rev. Lett. **35**, 799 (1975).

[51] E. Graf, D. Lee, and J. D. Reppy, Phase separation and the superfluid transition in liquid He^3-He^4 mixtures, Phys. Rev. Lett. **19**, 417 (1967).

[52] R. J. Birgeneau, G. Shirane, M. Blume, and W. C. Koehler, Tricritical-point phase diagram in $FeCl_2$, Phys. Rev. Lett. **33**, 1098 (1974).

[53] J. Griffin and S. Schnatterly, Optical measurement of the magnetic tricritical behavior of $FeCl_2$, Phys. Rev. Lett. **33**, 1576 (1974).

[54] J. F. Dillon, E. Y. Chen, and H. J. Guggenheim, Optical studies of the magnetic phase diagram of $FeCl_2$, Phys. Rev. B **18**, 377 (1978).

[55] H. T. Shang and M. B. Salamon, Tricritical scaling and logarithmic corrections for the metamagnet $FeCl_2$, Phys. Rev. B **22**, 4401 (1980).

[56] P. Leiderer, D. R. Nelson, D. R. Watts, and W. W. Webb, Tricritical slowing down of superfluid dynamics in ^3He - ^4He mixtures, Phys. Rev. Lett. **34**, 1080 (1975).

[57] N. Giordano, Experimental determination of the tricritical crossover exponent, Phys. Rev. B **14**, 2927 (1976).

[58] J.-Q. Yan, Y. H. Liu, D. S. Parker, Y. Wu, A. A. Aczel, M. Matsuda, M. A. McGuire, and B. C. Sales, A-type antiferromagnetic order in $MnBi_4Te_7$ and $MnBi_6Te_{10}$ single crystals, Phys. Rev. Mater. **4**, 054202 (2020).

[59] J. M. D. Coey, *Magnetism and Magnetic Materials* (Cambridge University Press, Cambridge, UK, 2010).

[60] K. H. J. Buschow, F. R. Boer *et al.*, *Physics of Magnetism and Magnetic Materials* (Springer, Berlin, 2003), Vol. 7.

[61] See Supplemental Material at http://link.aps.org/supplemental/10.1103/PhysRevB.109.214428 for the demagnetic field effect, $M(H)$ curves at different temperature, internal field vs temperature phase diagram, the tricritical scaling fitting, and typical ac susceptibility versus field with the different excitation frequency.

[62] R. Bidaux, P. Carrara, and B. Vivet, Antiferromagnetisme dans un champ magnetique I. traitement de champ moleculaire, J. Phys. C: Solid State Phys. **28**, 2453 (1967).

[63] A. F. G. Wyatt, Magnetization of dysprosium aluminium garnet, J. Phys. C: Solid State Phys. **1**, 684 (1968).

[64] J. F. Dillon, E. Y. Chen, N. Giordano, and W. P. Wolf, Time-reversed antiferromagnetic states in dysprosium aluminum garnet, Phys. Rev. Lett. **33**, 98 (1974).

[65] P. M. Sass, W. Ge, J. Yan, D. Obeysekera, J. J. Yang, and W. Wu, Magnetic imaging of domain walls in the antiferromagnetic topological insulator $MnBi_2Te_4$, Nano Lett. **20**, 2609 (2020).

[66] J. Guo, H. Wang, X. Wang, S. Gu, S. Mi, S. Zhu, J. Hu, F. Pang, W. Ji, H.-J. Gao, T. Xia, and Z. Cheng, Coexisting ferromagnetic–antiferromagnetic phases and manipulation in a magnetic topological insulator $MnBi_4Te_7$, J. Phys. Chem. C **126**, 13884 (2022).

[67] M. Twengström, L. Bovo, O. A. Petrenko, S. T. Bramwell, and P. Henelius, $LiHoF_4$: Cuboidal demagnetizing factor in an ising ferromagnet, Phys. Rev. B **102**, 144426 (2020).
[68] R. Pynn and A. Skjeltorp, *Multicritical Phenomena* (Springer Science & Business Media, New York, 2012), Vol. 106.
[69] C. Vettier, H. L. Alberts, and D. Bloch, Tricritical lines in metamagnets, Phys. Rev. Lett. **31**, 1414 (1973).
[70] I. S. Jacobs and P. E. Lawrence, Metamagnetic phase transitions and hysteresis in $FeCl_2$, Phys. Rev. **164**, 866 (1967).
[71] C. Binek and W. Kleemann, Domainlike antiferromagnetic correlations of paramagnetic $FeCl_2$: A field-induced griffiths phase?, Phys. Rev. Lett. **72**, 1287 (1994).
[72] W. Ge, J. Kim, Y.-T. Chan, D. Vanderbilt, J. Yan, and W. Wu, Direct visualization of surface spin-flip transition in $MnBi_4Te_7$, Phys. Rev. Lett. **129**, 107204 (2022).
[73] J. Kincaid and E. Cohen, Variation of the critical behavior in metamagnets, Phys. Lett. A **50**, 317 (1974).
[74] Y. Liu, L.-L. Wang, Q. Zheng, Z. Huang, X. Wang, M. Chi, Y. Wu, B. C. Chakoumakos, M. A. McGuire, B. C. Sales, W. Wu, and J. Yan, Site mixing for engineering magnetic topological insulators, Phys. Rev. X **11**, 021033 (2021).
[75] V. Ginzburg, A. Levanyuk, and A. Sobyanin, Light scattering near phase transition points in solids, Phys. Rep. **57**, 151 (1980).
[76] D. R. Nelson and M. E. Fisher, Renormalization-group analysis of metamagnetic tricritical behavior, Phys. Rev. B **11**, 1030 (1975).
[77] F. J. Wegner and E. K. Riedel, Logarithmic corrections to the molecular-field behavior of critical and tricritical systems, Phys. Rev. B **7**, 248 (1973).
[78] B. Chen, F. Fei, D. Zhang, B. Zhang, W. Liu, S. Zhang, P. Wang, B. Wei, Y. Zhang, Z. Zuo, J. Guo, Q. Liu, Z. Wang, X. Wu, J. Zong, X. Xie, W. Chen, Z. Sun, S. Wang, Y. Zhang *et al.*, Intrinsic magnetic topological insulator phases in the Sb doped $MnBi_2Te_4$ bulks and thin flakes, Nat. Commun. **10**, 4469 (2019).
[79] R. B. Griffiths, Proposal for notation at tricritical points, Phys. Rev. B **7**, 545 (1973).
[80] T. S. Chang, A. Hankey, and H. E. Stanley, Generalized scaling hypothesis in multicomponent systems. I. classification of critical points by order and scaling at tricritical points, Phys. Rev. B **8**, 346 (1973).
[81] A. Hankey, T. S. Chang, and H. E. Stanley, Generalized scaling hypothesis in multicomponent systems. II. Scaling hypothesis at critical points of arbitrary order, Phys. Rev. B **8**, 1178 (1973).
[82] J. W. Essam and M. E. Fisher, Padé approximant studies of the lattice gas and Ising ferromagnet below the critical point, J. Chem. Phys. **38**, 802 (1963).
[83] M. E. Fisher, The theory of equilibrium critical phenomena, Rep. Prog. Phys. **31**, 418 (1968).
[84] B. Widom, Degree of the critical isotherm, J. Chem. Phys. **41**, 1633 (1964).